PNAS RESEARCH ARTICLE | MICROBIOLOGY OPEN ACCESS

MITD1 is a brain-specific interferon-inducible factor that inhibits flavivirus replication

Jim Zoladek[a], Marion Cannac[a,b], Maël Seite[a], Emma Davies[c], Jordan Quellec[b,d], Jonathan Barthelemy[b], Kamila Gorna[e], Sophie Desgraupes[a], Ines Bribes[a], Sara Salinas[b], Muriel Coulpier[e], Nathalie J. Arhel[a], Massimo Palmarini[c], Yannick Simonin[b], Sam J. Wilson[c,f], and Sébastien Nisole[a,1]

Affiliations are included on p. 12.

Edited by Michael Diamond, Washington University in St. Louis School of Medicine, St. Louis, MO; received January 30, 2025; accepted February 19, 2025

West Nile virus (WNV) and Usutu virus (USUV) are closely related mosquito-borne neurotropic flaviviruses that share common transmission cycle and can infect humans. However, while human infections by WNV are widespread, infections by USUV are comparatively less frequent, less severe, and currently limited to Africa and Europe. To identify human host factors that contribute to the pathogenic signatures of these two flaviviruses, we carried out an arrayed expression screen of over 1,300 interferon-stimulated genes (ISGs). Several ISGs known to target flaviviruses, including IFI6, SHFL, and RTP4 were among the strongest hits. Interestingly, we also found MITD1, an ISG with no previously reported antiviral activity, among the strongest hits. We demonstrated that the antiviral activity of MITD1 was not limited to USUV and WNV, since it also inhibited Zika and dengue virus replication. We found MITD1 to interfere with viral RNA replication by sequestering specific endosomal sorting complexes required for transport-III (ESCRT-III) proteins involved in the formation of viral replication factories. MITD1 expression was not increased by type I interferon (IFN-I) in most human cells and mouse tissues that we examined, although WNV and USUV replication was strongly inhibited by IFN-I. Strikingly, MITD1 was induced in the brain of USUV-infected mice and importantly, in human monocyte-derived microglia. Using human microglial-like cells, we confirmed that MITD1 is an essential mediator of the anti-flavivirus activity of IFN-I in these cells. We conclude that MITD1 plays a key role in the cellular defenses against neurotropic flaviviruses.

flavivirus | interferon-stimulated genes | innate immune response | microglial cells

Significance

Mosquito-borne flaviviruses are emerging worldwide, posing a major threat to public health. In this work, we have identified an antiviral protein, named MITD1, which is able to block flavivirus replication in human cells. Specifically, MITD1 was found to prevent the formation of viral replication factories that flaviviruses establish within target cells. Strikingly, the expression of MITD1 is specifically induced in microglial cells, the main immune cells of the central nervous system, and prevents their infection. Given that most pathogenic flaviviruses can infect the brain and cause severe neurological disease, our data provide a better understanding of the molecular mechanisms underlying the physiopathology of neurotropic flavivirus infections.

Orthoflaviviruses (hereafter referred for simplicity as flaviviruses), a genus of positive-stranded RNA viruses belonging to the *Flaviviridae* family, include several viruses that increasingly threaten both human and animal health. Most human-pathogenic flaviviruses are transmitted horizontally between hematophagous arthropods (mainly mosquitoes and ticks) and vertebrate hosts (1). Once introduced into the skin during a blood meal, flaviviruses disseminate and replicate in various organs of the vertebrate host. These small, enveloped viruses have a 10 to 11 kb genome with a single coding sequence flanked by structured 5′ and 3′ untranslated regions. The coding sequence encodes a polyprotein consisting of three structural and seven nonstructural proteins. The flavivirus replicative cycle is well characterized (1, 2). Following interactions between viral envelope proteins and cell receptors, flaviviruses enter target cells via clathrin-dependent endocytosis. Low pH in late endosomes induces membrane fusion, releasing nucleocapsids into the cytoplasm, where uncoating occurs. The viral genome is translated into polyproteins, which are processed into individual proteins by viral and cellular proteases. Nonstructural proteins form replication factories within invaginated endoplasmic reticulum (ER) compartments to replicate viral RNA. Structural proteins are assembled and loaded with viral RNA in the ER, newly formed virions are matured in the Golgi complex, and viral progeny are released by exocytosis (1, 2).

Among mosquito-borne flaviviruses, dengue virus (DENV), yellow fever virus (YFV), Zika virus (ZIKV), and West Nile virus (WNV) are significant human pathogens, responsible for most arboviral diseases worldwide. However, other, lesser-known flaviviruses are emerging in all regions of the world, posing a growing threat to public health (1). This is the case of the Usutu virus (USUV), a neurotropic virus discovered in 1959 in South Africa, which was introduced into Europe in the early 2000s and has been spreading ever since (3–6). In Europe, USUV is responsible for major outbreaks in wild birds associated with massive mortality. Human infections have also been reported, some associated with severe neurological disorders (3–8). The prospect of USUV spreading further outside Europe was a cause of concern (9), considering that USUV closely resembles WNV, which

Author contributions: J.Z., S.S., M. Coulpier, N.J.A., M.P., Y.S., S.J.W., and S.N. designed research; J.Z., M. Cannac, M.S., E.D., J.Q., J.B., K.G., S.D., I.B., and S.N. performed research; S.J.W. and S.N. contributed new reagents/analytic tools; J.Z., M. Cannac, M.S., M. Coulpier, N.J.A., and S.N. analyzed data; and J.Z. and S.N. wrote the paper.

The authors declare no competing interest.

This article is a PNAS Direct Submission.

[1]To whom correspondence may be addressed. Email: sebastien.nisole@inserm.fr.

This article contains supporting information online at https://www.pnas.org/lookup/suppl/doi:10.1073/pnas.2502064122/-/DCSupplemental.

Published March 20, 2025.

caused a major epidemic in New York in 1999 and has since spread widely across North America (10, 11). These concerns were recently confirmed as USUV circulation was detected in South America, identified by RT-qPCR in nine symptomatic patients in Colombia (12). USUV and WNV are part of the Japanese encephalitis virus (JEV) serocomplex and share an enzootic cycle that involves wild birds and *Culex* mosquitoes (3–6).

USUV is generally less pathogenic than WNV, although it can rarely cause severe neurological symptoms in humans (3–6). The lower virulence of USUV may be due to the greater sensitivity of this virus to type I interferon (IFN-I) (13, 14), an antiviral cytokine secreted by infected cells that triggers the expression of hundreds of interferon-stimulated genes (ISGs) in infected and surrounding cells, helping them resist viral infections (15, 16).

In order to identify ISGs that inhibit USUV replication and compare them to those interfering with WNV, we screened over 1,300 ISGs from human, bovine, and simian origins. Among the hits identified, some ISGs were already known to inhibit flaviviral replication, including IFI6, SHFL, RTP4, ISG20, and SLFN11 (17–24). Unexpectedly, one of the strongest hits was an ISG with no previously reported antiviral activity, called MITD1 (microtubule interacting and trafficking domain containing 1). Interestingly, MITD1 not only blocked replication of USUV, but also WNV, DENV, and ZIKV. Here, we show how MITD1 exerts its antiviral activity by binding to and sequestering specific ESCRT (endosomal sorting complexes required for transport) proteins, preventing the formation of virus-induced ER membrane invaginations necessary for viral replication (25–29). MITD1 expression was specifically induced in the brain of mice infected with USUV and in microglial cells, brain-resident macrophages that are highly dependent on interferon to resist flavivirus infections (30).

Results

ISG-Expression Screens Identify MITD1 as a Restriction Factor for Flaviviruses. First, we assessed whether USUV and WNV had the same propensity to induce IFN-I and whether they had the same sensitivity to this antiviral defense. To this end, A549 cells were infected with either USUV (AF2 strain) or WNV (Lineage 2) at a MOI of 0.1 or 1 for 24 h. RT-qPCR quantification of IFN-β transcripts revealed that, although both viruses induced robust IFN-I synthesis, USUV triggered a greater response than WNV (Fig. 1*A*). This was confirmed by measuring the IFN-I levels in the supernatant of infected cells (Fig. 1*B*). As expected, this stronger IFN-I induction by USUV led to higher ISG expression, demonstrated by a greater MX1 induction in USUV-infected cells compared to WNV (Fig. 1*C*). We then assessed the sensitivity of USUV and WNV to the antiviral activity of IFN-I by treating A549 cells with increasing doses of IFN-I before infection. Viral RNA quantification at 24 h postinfection showed that USUV was more sensitive to IFN-I than WNV (Fig. 1*D*), consistent with previous studies (13, 14).

To identify antiviral effectors that interfere with USUV and WNV replication, we screened a library of lentiviral vectors encoding 570 human, 444 simian, and 314 bovine ISGs (24, 31, 32). Bovine and macaque ISG libraries contain orthologs and additional ISGs and were therefore included to increase the total number of ISGs under consideration (>1,000 in total, Fig. 1*E*). HEK 293T cells were transduced with lentiviral vectors coexpressing an ISG and red fluorescent protein (TagRFP) for 72 h, and then challenged with wild-type USUV or WNV for 48 h. Viral replication in TagRFP-negative and TagRFP-positive cells was assessed by flow cytometry using a pan-flavivirus anti-envelope antibody (Fig. 1*E*). The infection rate for each virus in the presence of each ISG was plotted as a percentage of the screen average (Fig. 1*F* and Dataset S1). As the data followed normal distribution, most ISGs had no impact on viral replication, but some showed significant deviation from the mean. Among the 38 statistically significant hits (z-score < −3 for human and z-score < −2 for macaque and bovine ISGs) were proteins involved in innate immune signaling, including DDX58, DDX60, STING-1, IRF1, IRF7, and STAT2 (33, 34), validating the accuracy of the screen.

The antiviral activity of the 13 best hits was confirmed in a secondary screen using 22 control genes for normalization and plotted as a two-dimensional dot-plot comparing USUV and WNV (Fig. 1*G*). Most genes inhibited both viruses equally, with exceptions including human SAMHD1, TRIM69, PARP12, PML, and ISG20. The latter being in line with our previous study (35). While most ISGs known to inhibit flavivirus replication, including IFI6, SHFL, and RTP4, were among the most effective against both viruses (19–22, 24), we also identified among the top hits an ISG with no previously reported antiviral activity, named MITD1 (microtubule interacting and trafficking domain containing 1). MITD1 was found to efficiently interfere with both WNV and USUV replication (Fig. 1*G*), but it should be noted that only the bovine ortholog of MITD1 was identified, as no human or simian orthologs were included in the ISG libraries.

Having observed that bovine MITD1 could impede both USUV and WNV replication, we aimed to assess its potential inhibitory activity on other mosquito-borne flaviviruses. To do so, we stably overexpressed bovine MITD1 in Vero E6 cells (Fig. 1 *H* and *I*) and infected them with USUV or WNV (as controls), as well as ZIKV (Asian lineage) and the four serotypes of DENV for 48 h. We found that MITD1 effectively blocks replication of ZIKV and all serotypes of DENV, with a similar efficacy (twofold to fourfold inhibition) to that observed for WNV and USUV (Fig. 1*J*), thus suggesting a broad anti-flavivirus activity of MITD1.

Furthermore, we investigated whether the human ortholog of MITD1 exhibits similar antiviral activity. To do so, HEK 293T cells overexpressing either bovine or human MITD1 orthologs, or E2 Crimson as a negative control (Fig. 1*K*), were infected with USUV or WNV for 48 h. Flow cytometry analysis revealed that both orthologs possessed a similar antiviral activity, leading to a twofold decrease of infected cells (Fig. 1*L*). This inhibition further resulted in more than 2-log reduction in viral titer, as determined by $TCID_{50}$ measurement in the supernatant of infected cells (Fig. 1*M*). Taken together, these data underscore the significant antiviral potential of MITD1 against multiple mosquito-borne flaviviruses.

MITD1 Inhibits Flavivirus Replication through an Indirect Mechanism. We aimed to determine at which stage of the viral infection cycle MITD1 acts. We first tested whether MITD1 overexpression interfered with the first steps of the infection (i.e., viral binding to the cell or endocytosis). We incubated Vero E6 cells overexpressing human MITD1 with WNV for 1 h at 4 °C to inhibit membrane trafficking, and viral binding was estimated by quantifying viral RNA by RT-qPCR (Fig. 2*A*). Heparin, a broad-spectrum inhibitor of viral binding to cells (36, 37), was used as a control. We observed that whereas heparin efficiently inhibited the binding of WNV at the cell surface, MITD1 overexpression had no effect (Fig. 2*B*). To determine whether endocytosis was affected by MITD1, we repeated the experiment, further incubating the cells for 2 h at 37 °C to enable endocytosis (Fig. 2*A*). After trypsinization to remove uninternalized viruses, intracellular viral RNA was quantified by RT-qPCR (Fig. 2*C*). PitStop2, an inhibitor of clathrin-dependent endocytosis (38, 39), was used as a control. Again, while PitStop2 completely blocked entry, MITD1 overexpression had no effect (Fig. 2*C*). As expected, similar results were obtained with USUV

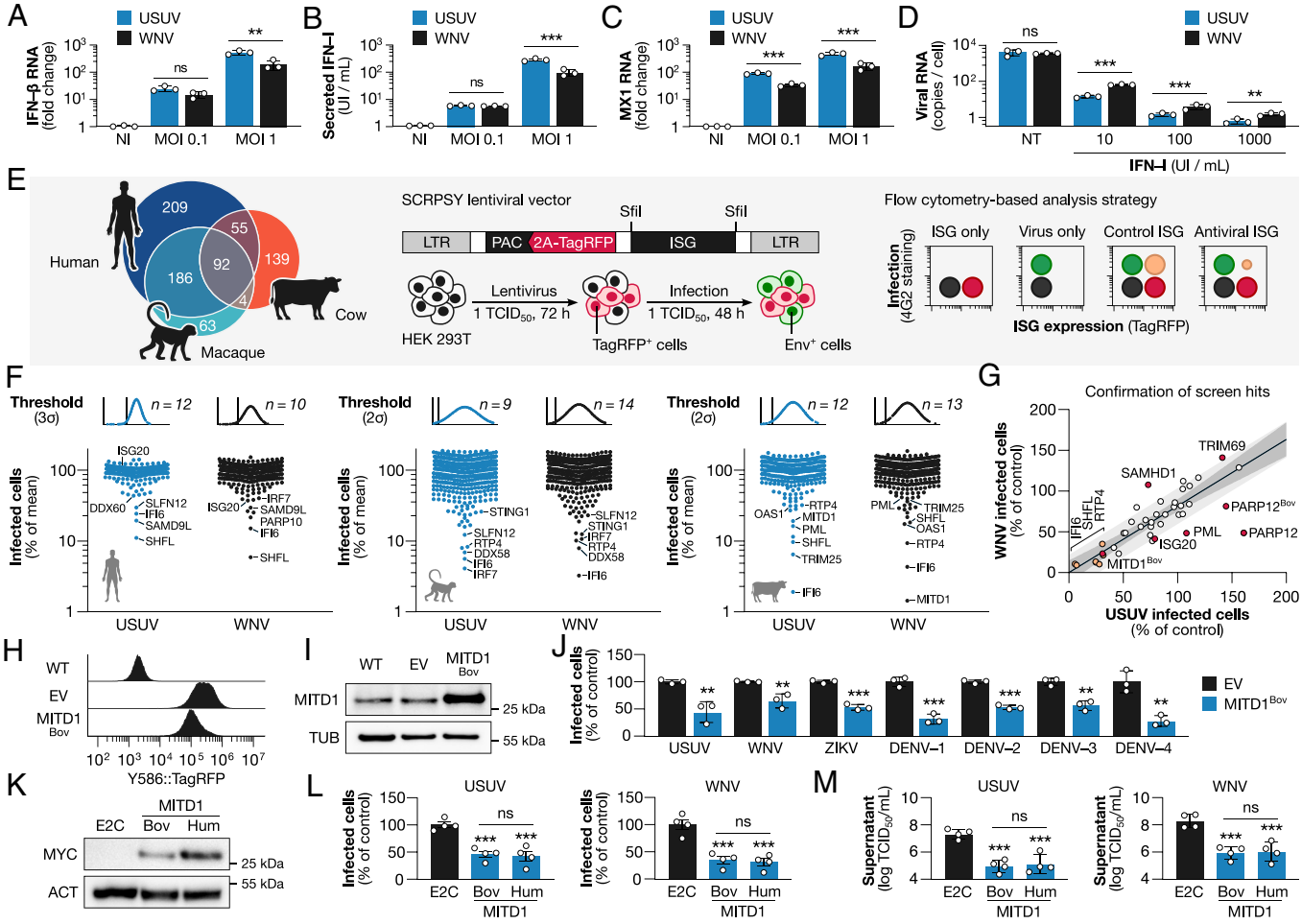

Fig. 1. ISG arrayed expression screen identifies MITD1 as a restriction factor for flaviviruses. (*A–C*) A549 cells were infected with USUV or WNV (MOI of 0.1 or 1) for 24 h. (*A*) IFN-β expression was assessed by RT-qPCR. (*B*) Secretion of IFN-I was quantified using STING-37 reporter cells. (*C*) MX1 expression was assessed by RT-qPCR. (*D*) A549 cells were treated with increasing concentration of IFN-I for 16 h, and infected with USUV or WNV (MOI of 0.1) for 24 h. Viral replication was assessed by RT-qPCR. (*E*) Venn diagram of the ISG libraries used in the screen, schematic of the SCRPSY lentiviral vector used for ISG delivery, and schematic of the flow cytometry screening strategy. (*F*) Normalized USUV or WNV infection (mean centered) of HEK 293T cells expressing ISGs. Each dot represents infection with a single ISG. The screen was performed once. (*G*) Confirmation screen of ISGs of interest, each dot representing the mean of two experiments. Gray areas indicate the 95% confidence (dark) and prediction (light) bands. (*H* and *I*) Generation of stable empty vector or bovine MITD1-expressing Vero E6 cells. (*H*) TagRFP expression was assessed by flow cytometry. (*I*) MITD1 expression was assessed by western blot. (*J*) Stable Vero E6 cells were infected with the indicated flaviviruses (MOI of 1) for 48 h; normalized infection (control centered) was assessed by flow cytometry. (*K*) Validation of transient expression of bovine and human MITD1 orthologs in HEK 293T cells at 24 h posttransduction, assessed by western blot. (*L* and *M*) E2 crimson, bovine or human MITD1-expressing HEK 293T cells were infected with USUV or WNV (MOI of 1) for 48 h. (*L*) Normalized infection (control centered), assessed by flow cytometry. (*M*) Viral production, assessed by $TCID_{50}$ titration. Data are presented as biological replicates and mean ± SD. ***$P \leq 0.001$; **$P \leq 0.01$; ns, $P > 0.05$. Statistical analyses: one-way ANOVA with Tukey's multiple comparisons test (*A–D*, *L*, and *M*) and two-tailed unpaired *t* tests (*J*). Data were log-transformed prior to analysis (*A–D*). Abbreviations: NI, not infected; NT, not treated; EV, empty vector; WT, wild type; E2C, E2 Crimson; PAC, puromycin N-acetyl transferase.

(*SI Appendix*, Fig. S1). Hence, we concluded that MITD1 inhibits flavivirus infection at a postentry step.

Next, to distinguish between an inhibition acting early (i.e., RNA replication) or late (i.e., assembly and budding) during the flavivirus replication cycle, we used a reporter viral particle (RVP) carrying a WNV-based replicon genome with the structural protein-coding region swapped with an eGFP reporter (Fig. 2*D*). These RVPs, generated by coexpressing the replicon genome with WNV structural proteins, allow infection and RNA replication that can be monitored by eGFP expression, but neither viral assembly nor release occurs (40). We used Vero E6 cells stably expressing human MITD1 or ISGs known to inhibit viral RNA replication (i.e., IFI6, SHFL, and RTP4; see Fig. 1*G*), and infected them with RVPs. The proportion of eGFP-positive cells was measured by flow cytometry. All tested ISGs, including MITD1, drastically decreased eGFP expression (Fig. 2*E*), indicating that MITD1 interferes with a postentry, but preassembly step, which may correspond to viral genome replication.

To further investigate the mechanism by which MITD1 is interfering with viral replication, we monitored dsRNA labeling (a marker of viral replication factories) in WNV-infected A549 cells at 24 h postinfection. Strikingly, there were significantly fewer dsRNA foci in MITD1-overexpressing cells (i.e., Myc-MITD1 positive) than in nontransduced cells (Fig. 2*F*), suggesting that MITD1 prevents the formation of viral replication factories. We also assessed the localization of endogenous MITD1 in infected cells by using a siRNA-validated antibody (*SI Appendix*, Fig. S2). While overlapping signals of endogenous MITD1 and dsRNA were observed in infected cells, no true colocalization suggested a recruitment of MITD1 to viral replication factories (Fig. 2*G*). This indicates that MITD1 antiviral activity is likely to be indirect.

MITD1 Interacts with CHMP1B and CHMP4B and Sequesters Them within Lipid-Rich Regions. The only previously reported function of MITD1 is during the last phases of mitosis, when it is recruited to midbodies by a subset of proteins from the ESCRT-III

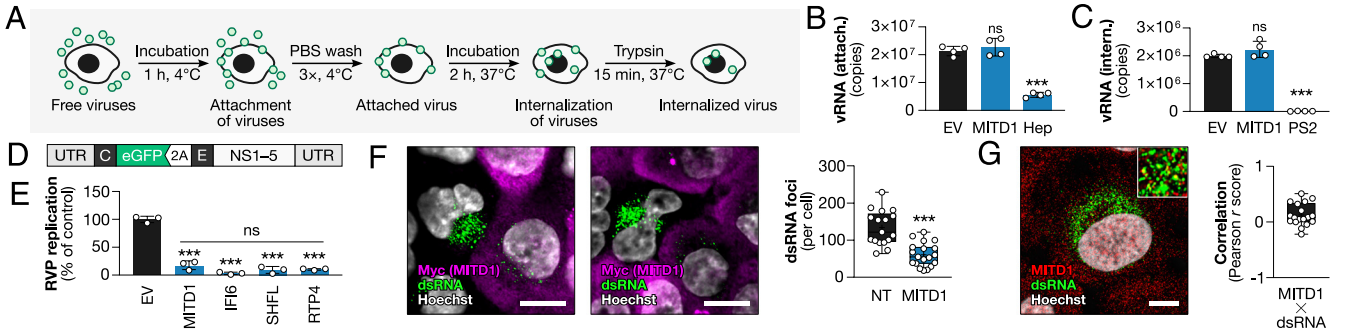

Fig. 2. MITD1 blocks flavivirus replication by an indirect mechanism. (*A–C*) Vero E6 cells stably expressing human MITD1 were infected with WNV (MOI of 20) for attachment and internalization assays. (*A*) Schematic of the assay. (*B*) WNV binding to MITD1-expressing cells, assessed by RT-qPCR; heparin at 200 µg/mL was used as control. (*C*) WNV entry into MITD1-expressing cells, assessed by RT-qPCR; PitStop2 at 50 µM was used as control. (*D*) Schematic of WNVII Rep genome replicon used to generate RVPs. (*E*) Stable MITD1-expressing Vero E6 cells were infected with WNV RVPs (MOI of 1) for 48 h. Normalized replication (eGFP fluorescence, control centered) was assessed by flow cytometry; stable IFI6, SHFL, and RTP4-expressing cells were used as controls. (*F*) A549 cells were transduced with 1 × $TCID_{50}$ of lentivectors expressing Myc-tagged MITD1 for 24 h, then infected with WNV (MOI of 5) for 24 h. The viral replication factories (dsRNA) in transduced cells or not were assessed by confocal microscopy and quantified. (Scale bar: 10 µm). (*G*) A549 cells were infected with WNV (MOI of 1) for 24 h. The colocalization of endogenous MITD1 with viral replication factories (dsRNA) was assessed by confocal microscopy and estimated by calculating a Pearson's correlation score. (Scale bar: 5 µm). Data are presented as biological replicates and mean ± SD. ***$P \leq 0.001$; ns, $P > 0.05$. Statistical analyses: one-way ANOVA followed by Tukey's multiple comparisons test (*B*, *C*, and *E*), two-tailed unpaired *t* test (*F*), and Pearson correlation score (*r*) calculated on linear (15 µm each) measurements of gray values (*G*). Abbreviations: NT, not transduced; EV, empty vector; vRNA, viral RNA; RVP, reporter viral particle.

machinery and enables abscission by activating ESCRT-III assembly to membranes (41, 42). The ESCRT-III subunits, together with the ESCRT-I and ESCRT-II complexes and ALIX protein promote membrane remodeling and fission in various cellular processes, including abscission, multivesicular body formation, and autophagy (43). MITD1 contains a microtubule-interacting and trafficking (MIT) domain, which allows direct interaction with certain ESCRT-III proteins, including CHMP1A, CHMP1B, CHMP2A, CHMP3, CHMP4A, CHMP4B, CHMP6, and IST1 (41, 42, 44).

Viruses have evolved to exploit the ESCRT machinery to their own advantage, in particular in the case of enveloped viruses which use it for budding (29, 45). The remodeling of cell membranes induced by viruses to replicate also requires the ESCRT machinery. For flaviviruses, some CHMP proteins, notably CHMP2 and CHMP4, are relocalized to endoplasmic reticulum (ER) invaginations where viral replication occurs and directly participate in the biogenesis of these viral replication factories (25). Given these observations and the fact that MITD1 can interact with several CHMP proteins, we hypothesized that MITD1 might inhibit flavivirus replication by preventing CHMP proteins from remodeling ER membranes. To test this, we examined the possible link between MITD1 expression, ESCRT-III protein localization, and viral replication factory formation. Possible candidates included ALIX, CHMP1B, CHMP2A, and CHMP4B, as these proteins are both partners of MITD1 (41, 42, 44), and involved in flavivirus replication (25–28).

We first examined the localization of ALIX, CHMP1B, CHMP2A, and CHMP4B by confocal microscopy in A549 cells overexpressing human Myc-tagged MITD1. We ensured a transfection efficiency of around 50%, thus allowing the visualization of both Myc-positive and Myc-negative cells in the same field. In nontransfected cells, ALIX, CHMP1B, CHMP2A, and CHMP4B labeling appeared as small dots in the cytoplasm. Interestingly, while MITD1 overexpression had no effect on the cellular distribution of ALIX and CHMP2A, it caused a dramatic relocalization of CHMP1B and CHMP4B. Indeed, in MITD1-overexpressing cells, CHMP1B aggregated as large cytoplasmic foci close to the nucleus, while CHMP4B formed condensed donut-shaped structures scattered throughout the cytoplasm (Fig. 3*A*). This MITD1-induced specific relocalization of CHMP1B and CHMP4B was particularly clear when quantifying the size of foci in MITD1-overexpressing cells (Fig. 3*B*). It should be noted that this phenomenon was also observed upon overexpression of the bovine ortholog of MITD1 (*SI Appendix*, Fig. S3), consolidating the hypothesis of a conserved antiviral mechanism between bovine and human MITD1.

During cytokinesis, MITD1 enables ESCRT-III proteins to be recruited to midbodies. More precisely, MITD1 interacts with ESCRT-III proteins through its MIT domain, and mediates their association with membranes via its phospholipase D-like domain (Fig. 3*C*) (41, 42). We therefore wondered whether, as during mitosis, MITD1 overexpression induces membrane anchoring of CHMP proteins. To test this hypothesis, we took advantage of Nile Red, a lipophilic dye that fluoresces red when associated with phospholipids and yellow when in lipid droplets (46, 47).

By confocal microscopy, we observed that MITD1 expression induced the association of CHMP1B and CHMP4B with phospholipids (Fig. 3*D* and *SI Appendix*, Fig. S4), therefore confirming their anchoring to membranes. Interestingly, we found that MITD1 induced a preferential relocalization of CHMP4B, but not CHMP1B, into donut-shaped structures, half of which were filled with a lipid droplet, while the others appeared empty (respectively "f" and "e"; Fig. 3*E* and *SI Appendix*, Figs. S5 and S6). It should be noted that no lipid droplet biogenesis was triggered by MITD1 overexpression (*SI Appendix*, Fig. S7), thus indicating that MITD1 induces the association of CHMP4B with preexisting lipid droplets.

We repeated these same experiments in another cell line (HEK 293T) and obtained the same results, namely the MITD1-induced specific relocalization of CHMP1B and CHMP4B to cell membranes, and the association of CHMP4B with lipid droplets (*SI Appendix*, Fig. S8). Given the efficiency of transgene expression in these cells, we pursued our mechanistic investigations in HEK 293T cells.

We then asked whether MITD1-induced association of CHMP1B and CHMP4B with cytoplasmic lipid-rich regions leads to depletion of the soluble pool of these two proteins. To do this, we analyzed the fate of ESCRT-III proteins by western blot in HEK 293T cells overexpressing Myc-tagged MITD1, or GFP as a control. Interestingly, no significant change in total protein level was observed following MITD1 overexpression when using a strong lysis buffer (SDS buffer) that solubilizes even membrane-anchored proteins (Fig. 3 *F*, *Left*). In contrast, when using a milder buffer (RIPA buffer) that preserves membrane integrity, we observed that MITD1 overexpression led to a specific decrease in the amount of CHMP1B and

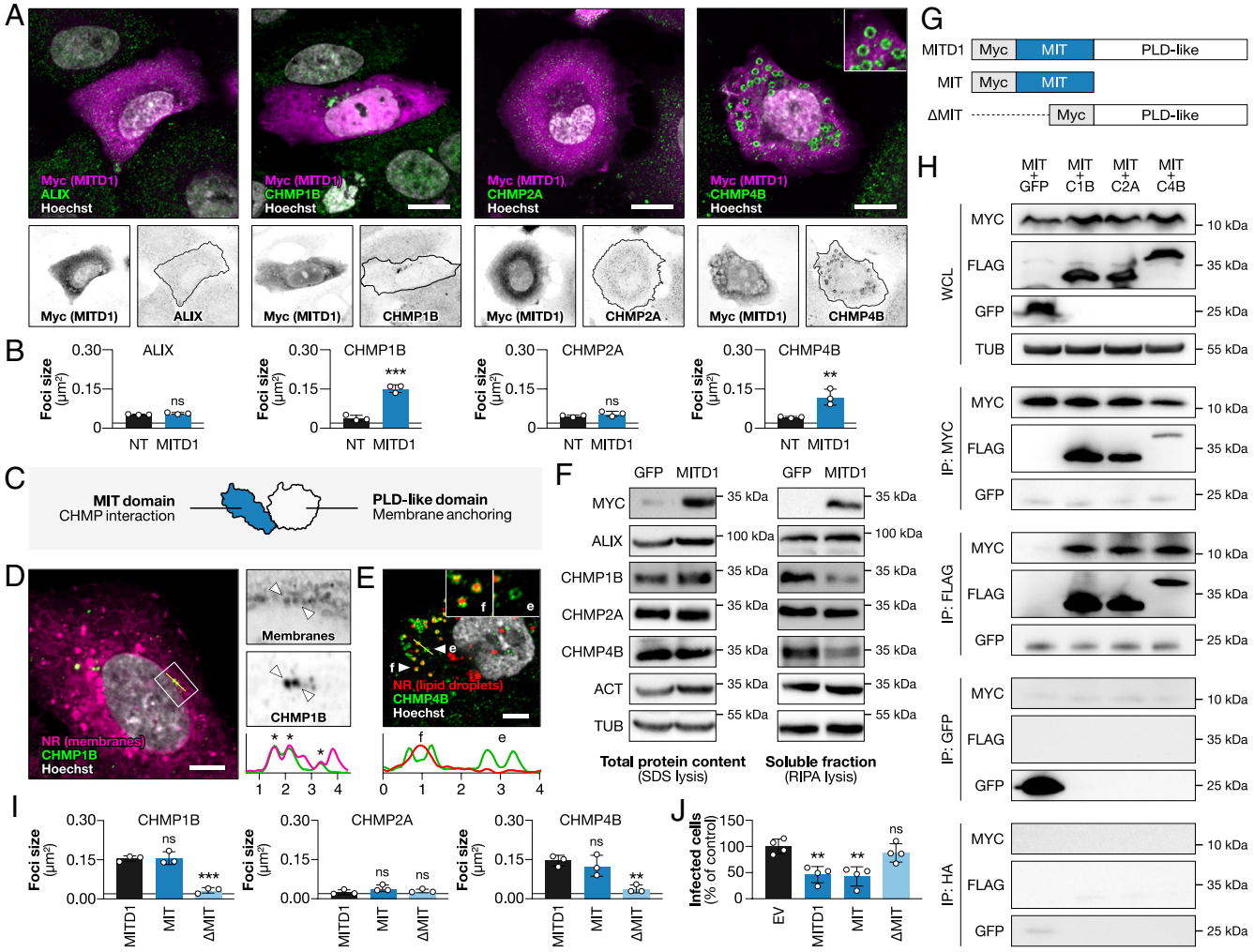

Fig. 3. MITD1 binds to and sequesters CHMP1B and CHMP4B within lipid-rich regions. (*A–E*) A549 cells were transfected with Myc-tagged MITD1 for 24 h. (*A*) Differential localization of ESCRT-III component proteins ALIX, CHMP1B, CHMP2A, and CHMP4B in transfected cells or not; assessed by confocal microscopy. MITD1 expression is outlined in black on the single channel fields. (Scale bar: 10 μm). (*B*) ESCRT-III component protein foci size alteration in MITD1-expressing cells was measured. (*C*) Schematic of the functional domains of MITD1. (*D*) Fate of CHMP1B aggregates in MITD1-expressing cells, compared to Nile Red phospholipid staining (561 nm excitation; 640/20 nm emission); assessed by confocal microscopy. Arrowheads indicate CHMP1B aggregates on the single channel fields. Cross-section gray value analyses corresponds to the yellow line. (Scale bar: 5 μm). (*E*) Fate of CHMP4B aggregates in MITD1-expressing cells, compared to Nile Red lipid droplet staining (514 nm excitation; 583/20 nm emission); assessed by confocal microscopy. Zooms show representative images of lipid-filled "f" and empty "e" aggregates. Cross-section analysis corresponds to the yellow line. (Scale bar: 5 μm). (*F*) Soluble ESCRT-III component proteins availability after MITD1 expression in HEK 293T cells, assessed by western blot. (*G*) Schematic of the Myc-tagged MITD1 individual domain constructs. (*H*) HEK 293T cells were cotransfected with Myc-tagged MIT domain of MITD1 and either GFP or FLAG-tagged CHMP1B, CHMP2A, and CHMP4B for 24 h. The interaction of ESCRT-III component protein with MIT domain of MITD1 was tested by immunoprecipitation with Myc, FLAG, GFP, or HA-Trap beads, and assessed by western blot. (*I*) HEK 293T cells were transfected with full-length or truncated Myc-tagged MITD1 constructs for 24 h. CHMP1B, CHMP2A, and CHMP4B foci size alteration in transfected cells was assessed by confocal microscopy and measured. (*J*) HEK 293T cells were transduced with lentivectors expressing full-length or truncated Myc-tagged MITD1 constructs for 24 h, then infected with WNV (MOI of 1) for 48 h. Normalized infection (control centered) was assessed by flow cytometry. Data are presented as biological replicates and mean ± SD. ***$P \le 0.001$; **$P \le 0.01$; ns, $P > 0.05$. Statistical analyses: two-tailed unpaired *t* tests (*B*) and one-way ANOVA followed by Tukey's multiple comparisons test (*H* and *I*). Abbreviations: NT, not transfected; EV, empty vector; NR, Nile Red; C1B, CHMP1B; C2A, CHMP2A; C4B, CHMP4B.

CHMP4B detected, without affecting the protein level of ALIX and CHMP2A (Fig. 3 *F*, *Right*). In line with our previous observations, this result confirms that MITD1 induces the relocation of soluble CHMP1B and CHMP4B proteins to membranes, thereby reducing the pool of soluble proteins.

To verify whether MITD1 induces membrane sequestration of CHMP1B and CHMP4B via a direct interaction through its MIT domain, we sought to confirm the interaction between these proteins. By immunoprecipitating the Myc-tagged MIT domain of human MITD1 ("MIT", Fig. 3*G*) with FLAG-tagged CHMP1B, CHMP2A, and CHMP4B, using GFP as a negative control (Fig. 3*H*), we confirmed that MITD1 interacts with CHMP proteins via its MIT domain. Furthermore, the deletion of the MIT domain of MITD1 ("ΔMIT", Fig. 3*G*) abrogated its ability to induce CHMP1B and CHMP4B relocalization (Fig. 3*I* and *SI Appendix*, Fig. S9) and to inhibit WNV (Fig. 3*J*) and USUV (*SI Appendix*, Fig. S10) replication, demonstrating that a direct interaction with CHMP1B and CHMP4B is necessary for MITD1 to exert its antiviral activity. In contrast, the antiviral activity of the MIT domain alone was comparable to that of the whole MITD1 protein, suggesting that the phospholipase D-like domain is not required (Fig. 3*J* and *SI Appendix*, Fig. S10).

CHMP1B and CHMP4B Participate in the Formation of Viral Replication Factories. Having elucidated the fate of CHMP1B and CHMP4B upon MITD1 overexpression, we sought to determine whether, as hypothesized, these proteins were involved in the formation of viral replication factories.

To this end, we first examined whether CHMPs colocalized with viral replication factories by proximity ligation assay (PLA),

a technique that allows in situ detection of protein interactions. We were able to confirm that CHMP1B, CHMP2A, and CHMP4B are located in the vicinity of viral replication foci in A549 infected with WNV for 24 h (Fig. 4 *A* and *B*). Expectedly, we did not observe any PLA signal between MITD1 and dsRNA foci (Fig. 4*A*), confirming our previous observations (Fig. 2*G*) which suggested that MITD1 acts remotely.

We then used RNA interference to reduce the available pool of CHMPs in infected cells, thus mimicking MITD1 activity. We used siRNAs to silence CHMP1B, CHMP2A, and CHMP4B in A549 cells, or PPIB as a negative control. After confirming knockdown efficiency by RT-qPCR and western blot (Fig. 4*C*), the cells were infected with WNV and viral replication was quantified by RT-qPCR (Fig. 4*D*). Although CHMP1B and CHMP4B knockdown significantly affected the level of viral transcripts, only CHMP4B knockdown resulted in a strong, twofold reduction (Fig. 4*D*). Cosilencing CHMP1B and CHMP4B, or CHMP2A and CHMP4B (*SI Appendix*, Fig. S11), confirmed the critical role of CHMP4B in viral replication, with CHMP1B playing a secondary role and CHMP2A showing no involvement (Fig. 4*E*). Virus titrations in cell supernatants confirmed the dramatic impact of CHMP1B or CHMP4B knockdown and especially CHMP1B/CHMP4B double-knockdown on WNV replication (*SI Appendix*, Fig. S12). Consistently, the same results were obtained with USUV infection (*SI Appendix*, Fig. S13).

Complementary confocal microscopy analyses corroborated these data, showing a significant decrease in the number of viral replication factories following CHMP1B or CHMP4B knockdown, but not CHMP2A knockdown (Fig. 4 *F* and *G*). In line with our RT-qPCR data, simultaneous CHMP1B and CHMP4B knockdown resulted in an even more pronounced decrease of viral replication factories (Fig. 4 *F* and *G*).

Finally, to confirm that MITD1 blocks viral replication via its ability to interact with, and relocalize, CHMP1B and CHMP4B, we overexpressed MITD1 in CHMP knockdown cells (*SI Appendix*, Fig. S14) and assessed viral replication by RT-qPCR. As expected, MITD1 lost its antiviral activity following CHMP1B or CHMP4B knockdown, but not CHMP2A knockdown (Fig. 4*H*). This was further confirmed by flow cytometry (*SI Appendix*, Fig. S15).

Taken together, our results therefore demonstrate that CHMP1B and CHMP4B are required for the formation of viral replication factories, and that MITD1 inhibits flavivirus replication by triggering the association of CHMP1B and CHMP4B with lipid-rich cytoplasmic regions, thereby sequestering them away from viral replication factories. Since CHMP4B is also a key factor in the replication of viruses from other families, including alphaviruses (48), we evaluated the potential susceptibility of Chikungunya virus and observed that MITD1 overexpression also blocked the replication of this virus in Vero E6 cells (*SI Appendix*, Fig. S16), suggesting a broader antiviral activity of MITD1.

MITD1 Is an Effector of the Anti-Flaviviral Activity of IFN-I in Microglial Cells. Following our exogeneous expression experiments, we planned to carry out knockdown experiments of endogenous

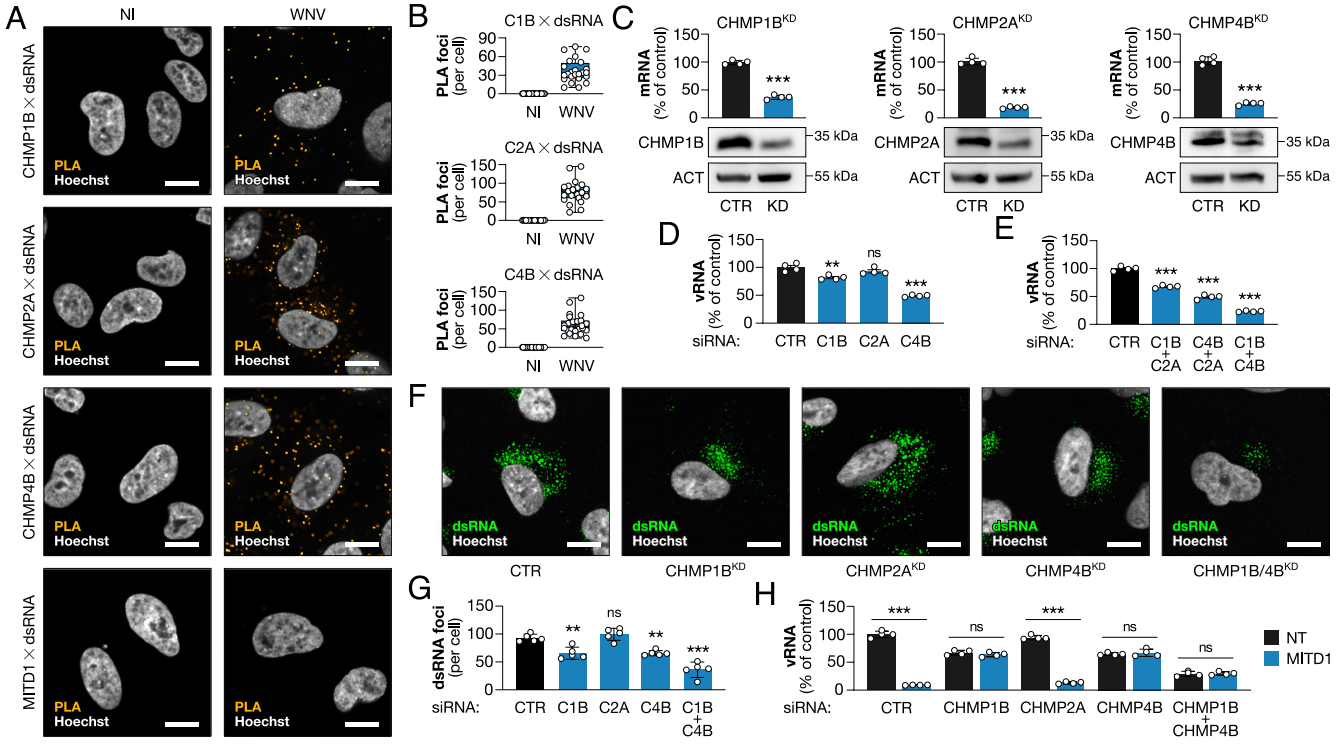

Fig. 4. Dysregulation of CHMP1B and CHMP4B blocks flavivirus replication. (*A* and *B*) A549 cells were infected with WNV (MOI of 5) for 24 h. (*A*) The interaction of dsRNA with CHMP1B, CHMP2A, CHMP4B, and MITD1 was tested with a proximity ligation assay (PLA) and assessed by confocal microscopy. (Scale bar: 10 μm). (*B*) PLA foci were quantified. (*C*–*G*) A549 cells were transfected with siRNAs targeting PPIB (as a control), CHMP1B, CHMP2A, or CHMP4B (alone or two together) for 24 h, then infected with WNV (MOI of 2) for 24 h. (*C*) Validation of single CHMP knockdowns, assessed by RT-qPCR and western blot. (*D*) Normalized viral RNA level (control centered) in single CHMP knockdown A549 cells infected with WNV, assessed by RT-qPCR. (*E*) Normalized viral RNA level (control centered) in double CHMP knockdown A549 cells infected with WNV, assessed by RT-qPCR. (*F*) Viral replication factories (dsRNA), assessed by confocal microscopy. (Scale bar: 10 μm). (*G*) The number of viral replication factories (dsRNA) per cell was quantified. (*H*) A549 cells were transfected with siRNAs targeting PPIB (as a control), CHMP1B, CHMP2A, and CHMP4B alone, or coupled CHMP1B/CHMP4B for 24 h, then transduced with lentivectors expressing MITD1 for 24 h, then infected with WNV (MOI of 1) for 24 h. Normalized viral RNA level (control centered) was assessed by RT-qPCR. Data are presented as biological replicates and mean ± SD. ***$P \leq 0.001$; **$P \leq 0.01$; ns, $P > 0.05$. Statistical analyses: two-tailed unpaired *t* tests (*C*), one-way ANOVA followed by Tukey's multiple comparisons test (*D*, *E*, and *G*), and two-way ANOVA followed by Šidák's multiple comparisons test (*H*). Abbreviations: NI, not infected; NT, not transduced; KD, knockdown; vRNA, viral RNA; C1B, CHMP1B; C2A, CHMP2A; C4B, CHMP4B.

IFN-induced MITD1 to confirm its physiological antiviral role. To do so, we first investigated the induction of MITD1 by IFN-I in different cell types. MITD1 and 28 other ISGs (including screen hits) were assessed in three classical human cell lines (A549, HT1080, and Huh7), primary human monocytes, monocyte-derived macrophages (MDMs), and monocyte-derived dendritic cells (MDDCs) treated with IFN-I for 16 h. Strikingly, MITD1 was the only ISG we tested not to be induced by IFN-I in any cell type (Fig. 5*A*). Given that MITD1 is constitutively expressed in most human cells, we attempted to assess whether its silencing would still promote viral replication in A549 cells. However, while the knockdown of SHFL, a potent anti-flavivirus ISG (Fig. 1*G*), enabled an effective rescue of WNV and USUV following IFN treatment, MITD1 knockdown did not, either in IFN-treated or untreated cells (*SI Appendix*, Fig. S17). This result therefore indicates that the steady-state expression level of MITD1 is not sufficient to confer resistance to infection.

We then examined whether MITD1 might be specifically induced by IFN-I in certain organs. To test this hypothesis, we quantified IFN-β and MITD1 transcripts in the liver, kidneys, spleen, and brain of mice infected with USUV for 6 d (Fig. 5 *B* and *C*). As a neurotropic virus, USUV had the highest number of viral transcripts in the brain, which also showed the highest IFN-β transcript levels, along with the spleen. Surprisingly, MITD1 expression was significantly higher in the brain of infected mice (Fig. 5*C*), suggesting it might be a brain-specific ISG. Supporting this hypothesis, a previous study showed an increased MITD1 expression in the brain of DENV-1-infected mice (49).

In order to determine whether MITD1 is specifically induced in a given cell type in the brain, we investigated its expression following IFN-I treatment in different human brain cell models, namely human neuronal/glial cells (hNGCs) differentiated from human neural progenitor cells (hNPCs), primary human astrocytes, and primary human monocyte-derived microglia-like cells (MDMis). Additionally, MDMis were compared with monocyte-derived macrophages (MDMs) from the same donors as a control (Fig. 5*D*). Following treatment of these cell models with IFN-I for 8 h, we quantified the transcripts for MITD1 and two control ISGs, MX1, and ISG15, by RT-qPCR. Surprisingly, whereas MX1 and ISG15 transcripts were induced in all cell types, MITD1 expression increased only in MDMis (Fig. 5*E*). This was particularly striking when comparing MDMs and MDMis from the same donors, as MITD1 induction by IFN-I was only observed when monocytes were differentiated into microglial-like cells and not into macrophages (Fig. 5*E*).

Once we had identified microglial cells as the only human brain cells in which MITD1 is induced by IFN-I, we aimed to confirm that the mechanism we had described A549 and HEK 293T cells could be transposed to this particular cell type. We started by using the human microglial cell line HMC3, which has the advantage of being transfectable and was recently used in an siRNA-based screen of anti-flavivirus ISGs (50).

We first examined the localization of CHMP1B, CHMP2A, and CHMP4B by confocal microscopy in Myc-tagged MITD1-overexpressing HMC3 cells. As before, we ensured a transfection efficiency of around 50%, in order to allow visualization of Myc-positive and Myc-negative cells in the same field. As in A549 (Fig. 3*A*) and HEK 293T cells (*SI Appendix*, Fig. S8), we observed that MITD1 overexpression did not affect CHMP2A localization, while it caused CHMP1B aggregation and the formation of CHMP4B donut-shaped structures in the cytoplasm (Fig. 6*A*). In these cells too, around half of these circular structures formed by CHMP4B surround lipid droplets (*SI Appendix*, Fig. S18), confirming that MITD1-induced CHMP behavior is similar in microglial

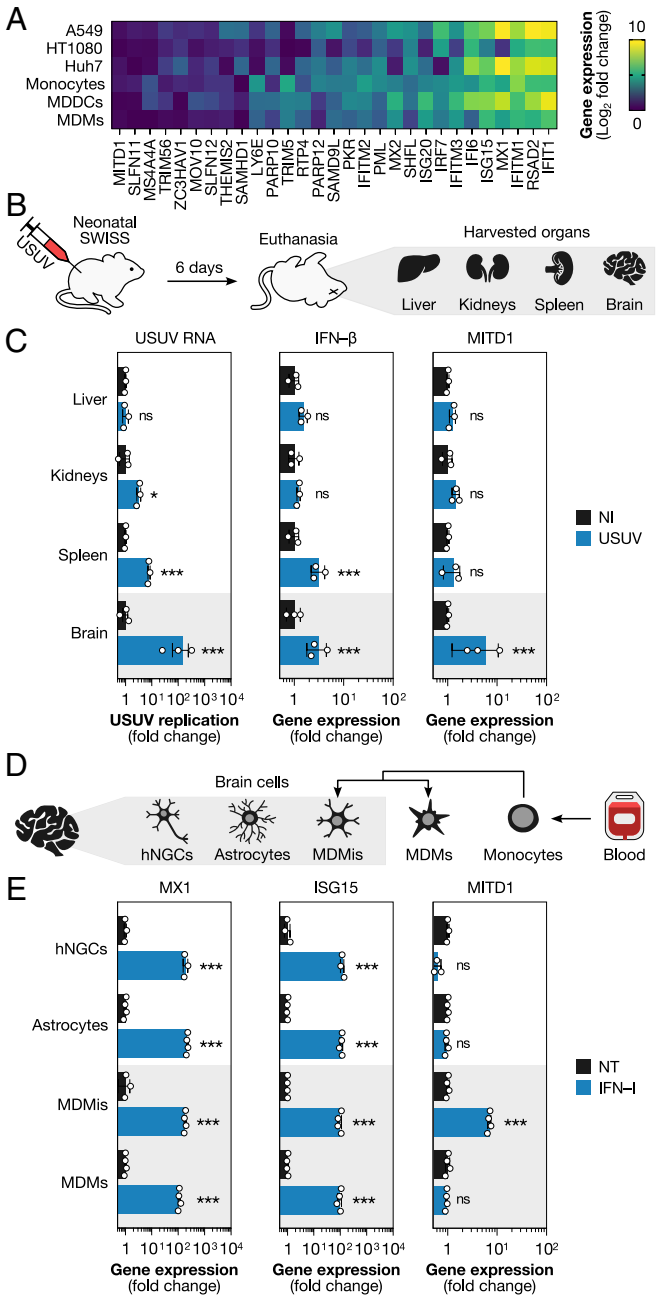

Fig. 5. MITD1 is a brain-specific ISG specifically induced in microglial cells. (*A*) A549, HT1080, Huh7, primary monocytes, MDDCs, and MDMs were treated with 100 UI/mL IFN-I for 16 h. Expression of the indicated genes was assessed by RT-qPCR. Genes are ordered from lower to higher mean induction. (*B*) Schematic of the mouse experiment pipeline with harvested organs. (*C*) Viral replication and expression of IFN-β and MITD1 transcripts in organs from control or USUV-infected mice, assessed by RT-qPCR. (*D*) Schematic representation of the simplified cell composition of the brain. (*E*) hNGCs, astrocytes, MDMis, and peripheral MDMs were treated with 100 UI/mL IFN-I for 8 h. MX1, ISG15, and MITD1 expression was assessed by RT-qPCR. Data are presented as biological replicates and mean ± SD. ***$P \le 0.001$; *$P \le 0.05$; ns, $P > 0.05$. Statistical analyses: two-way ANOVA followed by Šidák's multiple comparisons test (*E* and *C*). Abbreviations: NI, not infected; NT, not treated.

cells. We also confirmed that CHMP1B and CHMP4B were involved in the formation of viral replication factories in HMC3 cells. Indeed, as observed in A549 cells (Fig. 4*F*), knockdown of CHMP1B or CHMP4B, but not CHMP2A, significantly reduced the number of viral replication factories in WNV-infected cells (*SI Appendix*, Fig. S19).

Next, we used primary human MDMis to examine the fate of endogenous MITD1 and CHMPs proteins following WNV

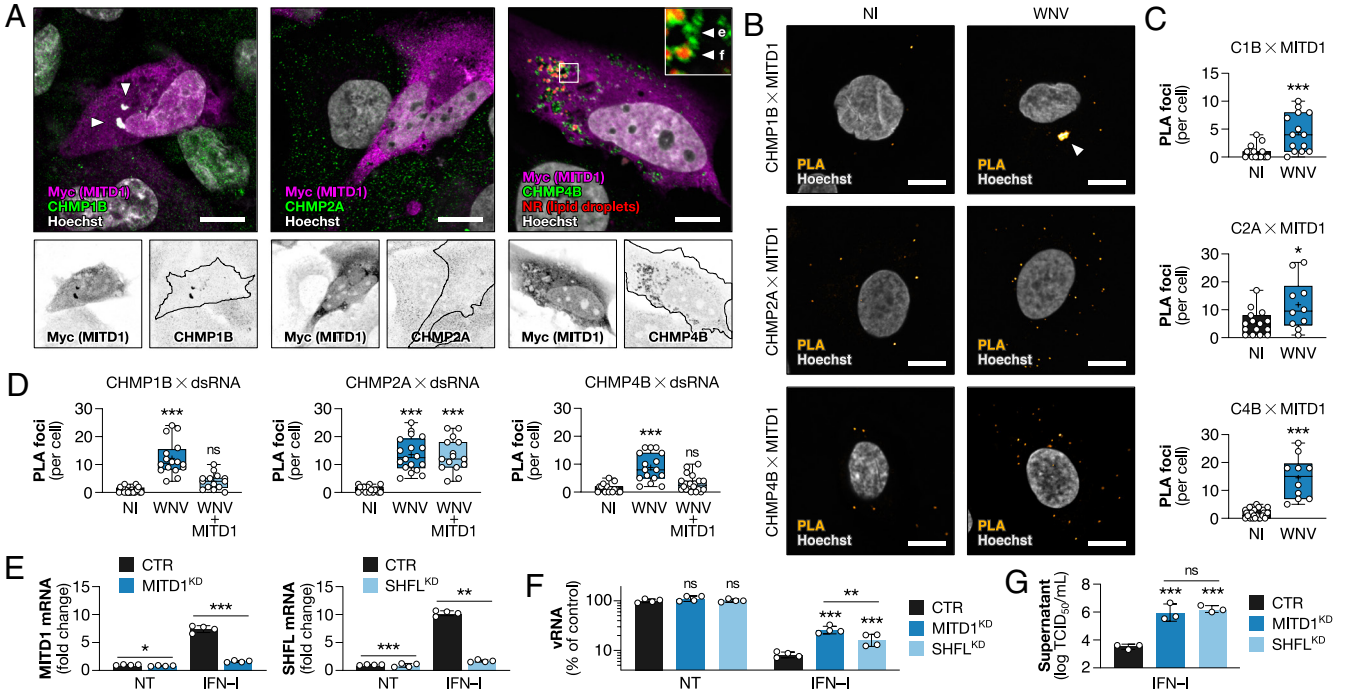

Fig. 6. MITD1 blocks flavivirus replication by sequestering CHMP1B and CHMP4B away from replication factories. (*A*) HMC3 cells were transfected with Myc-tagged MITD1 for 24 h. Differential localization of CHMP1B, CHMP2A, and CHMP4B in transfected cells or not was assessed by confocal microscopy. MITD1 expression is outlined in black on the single channel fields. Arrowheads indicate colocalization of MITD1 and CHMP1B. Fate of CHMP4B was further compared to Nile Red lipid droplet staining (514 nm excitation; 583/20 nm emission). (Scale bar: 10 μm). (*B*) MDMis were infected with WNV (MOI of 2) for 24 h. The interaction of CHMP1B, CHMP2A, and CHMP4B with MITD1 was tested with a proximity ligation assay (PLA) and assessed by confocal microscopy. Arrowheads indicate foci of MITD1 and CHMP1B condensation. (Scale bar: 10 μm). (*C*) PLA foci were quantified. (*D*) MDMis were transduced with lentivectors expressing MITD1 for 24 h, then infected with WNV (MOI of 2) for 24 h. The interaction of CHMP1B, CHMP2A, and CHMP4B with viral replication factories (dsRNA) was tested by PLA, assessed by confocal microscopy and quantified. (*E–G*) MDMis were transfected with siRNAs targeting MITD1 or SHFL for 24 h, and treated with 100 UI/mL IFN-I for 16 h. (*E*) Validation of MITD1 and SHFL knockdowns, assessed by RT-qPCR. (*F*) Control or IFN-I-treated MITD1^{KD} and SHFL^{KD} MDMis were infected with WNV (MOI of 1) for 24 h. Normalized viral replication (control centered) was assessed by RT-qPCR. (*G*) Viral production of IFN-I treated MITD1^{KD} and SHFL^{KD} MDMis, assessed by $TCID_{50}$ titration. Data are presented as biological replicates and mean ± SD. ***$P \le 0.001$; **$P \le 0.01$; *$P \le 0.05$; ns, $P > 0.05$. Statistical analyses: two-tailed unpaired *t* tests (*C* and *E*), one-way ANOVA followed by Tukey's multiple comparisons test (*D* and *G*), and two-way ANOVA followed by Šidák's multiple comparisons test (*F*). Data were log-transformed prior to analysis (*F*). Abbreviations: NI, not infected; NT, not treated; KD, knockdown; vRNA, viral RNA; C1B, CHMP1B; C2A, CHMP2A; C4B, CHMP4B.

infection. Using PLA, we observed that WNV infection caused MITD1 to recruit CHMP1B, CHMP2A, and CHMP4B, resulting in increased fluorescent foci in infected cells (Fig. 6 *B* and *C*). Interestingly, a large condensed cluster of CHMP1B and MITD1 can be observed in WNV-infected cells, which is reminiscent of the CHMP1B aggregates induced by MITD1 overexpression that we observed in A549 (Fig. 3*A*), HEK 293T (*SI Appendix*, Fig. S8), and HMC3 cells (Fig. 6*A*). Note that we obtained similar results with MDMis from another healthy donor (*SI Appendix*, Fig. S20).

We then investigated the proximity of CHMP proteins to viral RNA replication foci, in primary MDMis transduced or not with a lentiviral vector expressing MITD1. While CHMP1B, CHMP2A, and CHMP4B were localized in close proximity to replicating viral RNA, MITD1 specifically relocalized CHMP1B and CHMP4B away from viral replication factories, while CHMP2A remained in close proximity to viral RNA (Fig. 6*D* and *SI Appendix*, Fig. S21). Again, we obtained similar results with MDMis from another healthy donor (*SI Appendix*, Fig. S22). These observations confirm that MITD1 is able to sequester CHMP1B and CHMP2A away from viral replication factories in primary microglial cells.

Finally, we tested whether MITD1 was involved in the IFN-I-induced resistance of microglial cells to infection. To this end, we transfected MDMis with siRNAs targeting either MITD1, SHFL (as a positive control; see Fig. 1*G*), or a negative control siRNA targeting PPIB. Twenty-four hours posttransfection, cells were treated with IFN-I for 16 h to induce ISG expression. We verified by RT-qPCR the efficacy of IFN induction and siRNA-induced knockdown of MITD1 and SHFL (Fig. 6*E*). We then infected the cells with WNV for 24 h, and quantified viral RNA by RT-qPCR to assess infection. As expected, IFN-I treatment effectively suppressed WNV infection, and SHFL knockdown partially reversed its antiviral activity (Fig. 6*F*), confirming SHFL as a key ISG controlling flavivirus replication (19). Interestingly, MITD1 knockdown resulted in a similar, or greater, viral rescue than that of SHFL knockdown (Fig. 6*F*). Virus titrations in cell supernatants corroborated these results for two different donors (Fig. 6*G* and *SI Appendix*, Fig. S23). The exact same results were obtained with USUV infection (*SI Appendix*, Fig. S24), thus demonstrating that in microglial cells, MITD1 is a major effector of the antiviral activity of IFN-I toward neurotropic flaviviruses.

Discussion

Mosquito-borne flaviviruses are a growing threat to global public health. Among them, DENV alone threatens almost half the world's population, infecting around 400 million people per year. Other major human pathogens include ZIKV, WNV, and YFV. Emerging flaviviruses such as JEV and USUV are also becoming a concern in different parts of the world (1), highlighted by the recent emergence of USUV in America (12). All these flaviviruses are transmitted to humans by the bite of an infected mosquito, making the skin the first organ to encounter the virus. The interferon (IFN) response is an important defense mechanism against viral infections, which limits, if not prevents, the spread of viruses throughout the body. IFN is a cytokine that modulates multiple aspects of immunity and triggers an antiviral state in surrounding cells by stimulating the

synthesis of antiviral proteins encoded by ISGs. The speed of the IFN response and the effectiveness of the ISG products in thwarting viral replication are key factors in limiting the dissemination of the virus to the rest of the organism (15, 16).

Among the hundreds of ISGs, only a few can block a given virus, and numerous studies have identified the main effectors of the IFN-induced restriction of flavivirus replication. The most effective ISGs identified include IFI6, IFITMs, RSAD2, SHFL, RTP4, ISG20, and SLFN11 (17–24, 35). While ISGs that interfere with DENV, ZIKV, or WNV are well characterized, less is known about those affecting less-studied flaviviruses such as USUV.

Using an ISG screening approach, we identified MITD1 as a key ISG controlling mosquito-borne flavivirus replication, which proved capable of inhibiting replication of ZIKV, DENV, WNV, and USUV.

Our mechanistic studies revealed that MITD1 prevents the formation of virus-induced ER membrane invaginations by specifically binding and sequestering certain ESCRT-III proteins, including CHMP1B and CHMP4B. This mechanism, though not identical, is reminiscent of that of IFI6, an ISG-induced ER-resident protein that also blocks viral replication factory formation (20). However, IFI6 does not act through ESCRT or viral proteins but interacts with endoplasmic reticulum chaperone BiP (20). Unlike IFI6, MITD1 localization is not restricted to the ER and, given the importance of ESCRT-III proteins in the replication of all viruses, particularly for the budding of enveloped viruses (29, 45), our findings suggest that MITD1 may have a much broader antiviral activity. Our preliminary results with Chikungunya virus, an alphavirus, support this hypothesis, but further research will be needed to confirm this hypothesis and define the antiviral spectrum of MITD1.

It is very unlikely that MITD1 could have been identified in a loss-of-function screen due to its essential role in mitosis. It also would have been missed in a library of human ISGs, as it is not induced by interferon in most human cell types. The reason why we were able to identify the bovine form of MITD1 as a potent anti-flavivirus factor is that it was incorporated into the bovine ISG library (32), on the basis of a study comparing IFN-I-induced genes in different animal species, which identified MITD1 as an ISG in primary fibroblasts isolated from bovine skin samples (51).

While IFN induction of MITD1 has been described in bovine fibroblasts, we found that this was not the case in most human cells. In mice infected with USUV (this study) or DENV (49), MITD1 expression is only induced in the brain upon flavivirus infection. Furthermore, using various human brain cell models, we showed that IFN-I only induced MITD1 expression in microglial cells.

The IFN-I response can be locally activated in the central nervous system and is crucial for protecting the brain against neurotropic flaviviruses (52–54). However, whereas neurons are the main targets of flaviviruses in the brain, IFN seems particularly important in protecting microglia from infection. Indeed, a study showed that in wild-type mice infected with Langat virus, most infected brain cells were neurons, with only around 4% of infected cells being microglial cells. However, in IFNAR$^{-/-}$ mice, around 50% of infected cells were microglial cells, indicating that IFN plays a crucial role in the resistance of microglial cells to flaviviruses (30). Our results suggest that MITD1 could be one of these IFN-induced antiviral defenses conferring microglial cells with strong resistance to neurotropic flaviviruses.

Given the essential role of microglia in protecting the brain against viral infections, as demonstrated in the case of WNV and JEV (55, 56), MITD1 is likely to play a key role in the physiopathology of neurotropic flavivirus infections.

However, why MITD1 expression is only induced in microglial cells remains an open question. Gene expression under IFN stimulation is known to vary across cell types and also depends on IFN-stimulated response elements found within ISG promoters (57, 58). It has recently been shown that while STAT1 and STAT2 can bind to the MITD1 promoter, this is not the case for IRF9 (59). It is therefore possible that the absence of IRF9 makes it impossible to induce MITD1 expression in most cell types, with the exception of microglial cells. But further studies will be needed to confirm this hypothesis and understand the reasons for this cell specificity.

Materials and Methods

Cell Culture. A549, STING-37 (60), HEK 293T, Vero E6, HT1080, Huh7, and BHK 21 cells were cultured in high-glucose Dulbecco's modified Eagle's medium (DMEM, Gibco) supplemented with 10% fetal bovine serum (FBS, Serana), and 1% Penicillin/Streptomycin (Gibco). C6/36 cells were cultured in Leibovitz's L15 medium (Gibco) supplemented with 10% FBS, 1% Penicillin/Streptomycin, 1% typtose phosphate broth (Gibco), and 1% nonessential amino acids (Gibco).

Human neural progenitors (hNPCs) were cultured on matrigel-coated plates, as previously described (61). Differentiation into neuronal and glial cells (hNGCs) was induced 24 h after plating by replacing N2A medium with a 1:1 mix of N2A and NBC media and withdrawing EGF (TEBU) and bFGF (TEBU). N2A medium consisted of advanced DMEM-F12 supplemented with 2 mM L-glutamine, 0.1 mg/mL apotransferrin, 25 µg/mL insulin, and 6.3 ng/mL progesterone. NBC medium consisted of neurobasal medium supplemented with 2 mM L-glutamine and 1X B-27 supplement without vitamin A (Invitrogen).

Primary human astrocytes were purchased from ScienCell (San Diego, CA), and cultured on poly-D-lysine-coated plates in complete Astrocyte Medium (ScienCell). Cells were used at passage 3.

Buffy coats from healthy donors were obtained from the Etablissement Français du Sang (EFS, Montpellier, France). PBMCs were isolated by density centrifugation using Lymphoprep medium (STEMCELL Technologies) and cultured in RPMI (Gibco) supplemented with 10% FBS and 1% Penicillin/Streptomycin. Monocytes were isolated from PBMCs by plastic adhesion for 45 min and subsequently differentiated into monocyte-derived dendritic cells (MDDCs, *SI Appendix*, Fig. S25), monocyte-derived macrophages (MDMs, *SI Appendix*, Fig. S26), or monocyte-derived microglia-like cells (MDMis, *SI Appendix*, Fig. S27). MDDCs were differentiated in culture medium supplemented with 100 ng/mL IL-4 (CytoBox Mo-DC, Miltenyi) and 50 ng/mL GM-CSF (Gentaur) for 7 d. MDMs were differentiated in culture medium supplemented with 50 ng/mL GM-CSF for 10 d. MDMis were differentiated in culture medium supplemented with 10 ng/mL GM-CSF, 10 ng/mL M-CSF (PeproTech), 100 ng/mL CCL2 (PeproTech), 10 ng/mL NGF-β (PeproTech), and 100 ng/mL IL-34 (PeproTech) for 10 d.

All cells were kept at 37 °C with 5% CO_2 except C6/36 cells which were kept at 28 °C with no CO_2.

Viruses. Usutu virus (USUV) Africa 2 (Rhône2705/France/2015, GenBank accession no. KX601692) and West Nile virus (WNV) lineage 2 (WNV-6125/France/2018, GenBank accession no. MT863560) were provided by ANSES (National Agency for Food, Environmental and Occupational Health Safety, France). Dengue virus 1 (UVE/DENV-1/2012/VC/16692), dengue virus 2 (UVE/DENV-2/2014/FR/CNR_26104), dengue virus 3 (UVE/DENV-3/2015/TH/7716), dengue virus 4 (UVE/DENV-4/2014/HT/6169), and Zika virus (H/PF/2013, GenBank accession no. KJ776791) were kindly provided by Xavier de Lamballerie (Unité des Virus Emergents, Aix Marseille Université, Marseille, France), through the European Virus Archive GLOBAL (EVA-GLOBAL) project.

Viruses were amplified on 80% confluent C6/36 cells for 2 h, the inoculum was then removed, fresh medium was added, and supernatants containing viruses were collected when cytopathic effect was assessed and stored at −80 °C. Viral titers were determined by $TCID_{50}$ as described further.

The Chikungunya-mCherry virus was generated from an infectious clone derived from an Asian genotype of Chikungunya virus previously described (62), and kindly provided by Andres Merits (University of Tartu, Estonia). Briefly, HEK 293T cells were transfected with the infectious clone to produce the viruses, which were propagated on BHK 21 cells. The supernatant was collected, aliquots were stored at −80 °C, and titrated by plaque assays on Vero E6 cells.

Infections were conducted by inoculating cells with a low volume of viral dilution, at an appropriate multiplicity of infection (MOI) as detailed in figure legends, in serum-free DMEM for 2 h. The inoculum was then removed, cells were washed with 1× phosphate-buffered saline (PBS, Gibco), and cultured in fresh DMEM, 2% FBS, 1% Penicillin/Streptomycin.

WNV Reporter Virus Particles (RVPs). The constructs (WNVII Rep-G/Z and WNV NY99 CprME) used to generate the eGFP-encoding WNV RVPs were a kind gift of Theodore Pierson (Vaccine Research Center, National Institute of Allergy and Infectious Diseases, NIH, Bethesda, MD). RVP production was performed as described previously (40). Briefly, HEK 293T cells were transfected with the plasmids encoding the replicon (WNVII Rep-G/Z) and the WNV structural proteins (WNV NY99 CprME) using polyethylenimine (PEI, Polysciences) in a 3:1 (structural:replicon) ratio. RVP-containing supernatants were harvested 48 h posttransfection, filtered, concentrated by ultracentrifugation at 60,000 × g on an Optima XE-90 centrifuge with a SW 32 Ti rotor (Beckam Coulter), and stored at −80 °C.

RT-qPCR. Intracellular RNAs were extracted using the RNeasy Mini kit (Qiagen) following the manufacturer's instructions. Concentration and purity were evaluated by spectrophotometry (NanoDrop 2000c, Thermo Fisher Scientific). 500 ng of RNA were reverse transcribed with both oligo dT and random primers using the PrimeScript RT Reagent Kit (Perfect Real Time, Takara Bio Inc.) in a 10 μL reaction. Real-time PCRs were performed in duplicate using Takyon ROX SYBR Master Mix blue dTTP (Eurogentec) on an Applied Biosystems QuantStudio 5 (Thermo Fisher Scientific).

Cellular transcripts were quantified with primers which hybridize the cDNA sequences and viral genomes were quantified with primers within the 3′-untranslated region (*SI Appendix*, Table S1). Plasmids into which USUV and WNV amplicons have been cloned were used for absolute quantification of viral cDNA (*SI Appendix*, Fig. S28). Quantifications were performed with the following program: 3 min at 95 °C, 40 cycles of 15 s at 95 °C, 20 s at 60 °C and 20 s at 72 °C. Melting curves were also assessed.

Flow Cytometry. To quantify flavivirus infection, cells were detached with 0.25% Trypsin–EDTA (Gibco) treatment for 5 min, pelleted for 5 min at 500 × g, washed with PBS, pelleted, then fixed with PBS, 4% paraformaldehyde (PFA, Thermo Fisher Scientific) for 15 min. Cells were then permeabilized and saturated in FACS buffer: PBS, 1% bovine serum albumin (BSA, Thermo Fisher Scientific) and 0.05% saponin (Thermo Fisher Scientific) for 30 min. Cells were stained with anti-Envelope antibody (*SI Appendix*, Table S2) in FACS buffer for 2 h, washed twice with PBS, incubated with fluorescent secondary antibody (*SI Appendix*, Table S2) in FACS buffer for 1 h. Cells were washed once more, resuspended in PBS, and analyzed.

For MDDC, MDM, and MDMi phenotyping, cells were detached with PBS, 5 mM EDTA (Invitrogen) treatment for 10 min, pelleted for 5 min at 500 × g, washed with PBS, pelleted, then fixed with PBS, 4% PFA for 10 min. Cell surface was then stained with fluorescent antibodies (*SI Appendix*, Table S2) in PBS, 1% FBS, and Fc Block (BD Biosciences) for 30 min at 4 °C, cells were washed with PBS, pelleted, resuspended in PBS, and analyzed.

Myc-tagged transgene expression was assessed with anti-Myc primary antibody and fluorescent secondary antibody in FACS buffer (*SI Appendix*, Table S2). Reporter fluorescent proteins (TagRFP, E2 Crimson, eGFP, mCherry) were measured directly.

Lipid droplet quantity was assessed by incubating the cells with 1 μg/mL Nile Red (Thermo Fisher Scientific) or 2 μM Bodipy 493/503 (Thermo Fisher Scientific) for 15 min.

To monitor viral infections (except Chikungunya virus), transgene expression, and lipid droplet quantification, flow cytometry was performed on a Novocyte flow cytometer (Agilent), and data analysis was performed using Novoexpress software (Agilent). For phenotyping primary cells and quantifying Chikungunya virus infections, flow cytometry was performed on an LSR Fortessa (BD Biosciences) flow cytometer and results were analyzed with FlowJo (BD Biosciences).

Virus Titration. Cell supernatants containing viruses were collected and kept at −80 °C. Titers were obtained by $TCID_{50}$ using the Spearman–Kärber method. Briefly, confluent monolayers Vero E6 cells seeded on a 96-well plate were exposed to 10-fold serial dilutions of the supernatants, in triplicate, for 5 d. Cytopathic effect was assessed by direct contrast-phase microscopy on an EVOS M5000 (Thermo Fisher Scientific) imaging system (*SI Appendix*, Fig. S29).

Interferon Production Titration. Cell supernatants were collected and kept at −80 °C. Interferon was quantified on STING-37 cells that express the luciferase reporter under an ISRE (interferon-sensitive response element) promoter (60). Briefly, confluent monolayers of STING-37 cells were exposed to the supernatants for 24 h in triplicate. 10-fold serial dilution of Universal IFN-I (PBL Assay Science) was used for standard curve determination (*SI Appendix*, Fig. S30). Luciferase substrate (Bright-Glo, Promega) was added directly into the wells and luciferase activity was measured on an Infinite M Plex (TECAN) operated by Tecan i-control software.

Cell Stimulation with Interferon. To induce ISG expression, cell monolayers were treated with 10, 100, or 1,000 U/mL of universal IFN-I, from an original pool at 1×10^6 U/mL for 16 h, then washed with PBS. When cells were further infected, IFN-I was kept during the whole infection process.

ISG Arrayed Expression Screen. ISG library was produced as previously described (63). Briefly, ISG-encoding lentiviral vectors were generated by cotransfection of HEK 293T cells using PEI with HIV-1 Gag-Pol and VSV-G expression vectors, along with human, macaque, or bovine SCRPSY-based ISG expression vectors. Supernatants containing the lentiviral vectors were collected 48 h posttransfection and kept at −80 °C. Lentiviral vectors were mixed with an equal volume of fresh DMEM, 2% FBS, 12 μg/mL DEAE-Dextran (Thermo Fisher Scientific), incubated for 10 min, and then added on HEK 293T cells for 72 h. TagRFP expression was confirmed on an EVOS M5000 imaging system. The cells were then infected with 1 × $TCID_{50}$ of wild-type USUV or WNV for 48 h. Viral replication in TagRFP-negative and TagRFP-positive cells was assessed by flow cytometry as previously described (63).

Molecular Cloning of MITD1. Bovine MITD1 was obtained from the SCRPSY library. Human MITD1, cloned into pDONR 221 vector, was obtained from Montpellier Genomic Collections (MGC, France). pRRL-SFFV-E2Crimson-IRES-Puro was a kind gift of Olivier Moncorgé (Interferon and antiviral restriction team, IRIM, France).

Both orthologs of MITD1, and human MITD1 MIT and PLD-like domains were amplified with a N-terminal Myc tag by extension PCR using Q5 high fidelity DNA polymerase (New England Biolabs) and the appropriate primers (*SI Appendix*, Table S3) with the following program: 30 s at 98 °C followed by 30 cycles of 10 s at 98 °C, 20 s at 62 °C and 20 s at 72 °C. Final extension was allowed for an additional 2 min. PCR products were purified (NucleoSpin Gel and PCR Clean-up, Macherey-Nagel) and cloned into pcDNA3.1(+) and pRRL-SFFV-E2Crimson-IRES-Puro backbones by BamHI and NotI digestion (New England Biolabs), followed by T4 DNA ligation (New England Biolabs) following the manufacturer's instructions.

The resulting products (pCDNA3.1-Myc-MITD1^{Hum}, pRRL-SFFV-Myc-MITD1^{Hum}, pCDNA3.1-Myc-MITD1^{Bov}, pRRL-SFFV-Myc-MITD1^{Bov}, pCDNA3.1-Myc-MIT, pRRL-SFFV-Myc-MIT, pCDNA3.1-Myc-ΔMIT, and pRRL-SFFV-Myc-ΔMIT) were amplified on NEB 5-alpha bacteria (New England Biolabs) and constructs were controlled by whole plasmid sequencing (Plasmidsaurus).

Gene Overexpression. pcDNA3.1-CHMP1B-FLAG was ordered from GenScript (#OHu09157D). pcDNA3.1-CHMP2A-FLAG and pcDNA3.1-CHMP4B-FLAG were a kind gift of Cécile Boscheron and Winfried Weissenhorn (Institut de Biologie Structurale, Grenoble, France). pMD2.G (#12259) and pCMVR8.74 (#22036) were obtained from Addgene.

Stable MITD1 overexpression in Vero E6 cells was achieved using lentiviral vectors. Either empty SCRPSY and SCRPSY-MITD1^{Bov}, or pRRL-SFFV-E2Crimson and pRRL-SFFV-Myc-MITD1^{Hum} were cotransfected with pMD2.G and pCMVR8.74 in HEK 293T cells using PEI. Supernatants were harvested 48 h posttransfection. HEK 293T or Vero E6 cells were exposed to the lentivector-containing supernatants for 72 h and treated with puromycin for 14 d, with additional cell sorting on a FACSAria II (Becton Dickinson).

Transient MITD1 overexpression was also achieved using lentiviral vectors. Briefly, pRRL-SFFV-Myc-MITD1^{Hum}, pRRL-SFFV-Myc-MITD1^{Bov}, pRRL-SFFV-Myc-MIT, pRRL-SFFV-Myc-ΔMIT, and pRRL-SFFV-E2Crimson were cotransfected with pMD2.G and pCMVR8.74 in HEK 293T cells using PEI. Supernatants were harvested 48 h posttransfection, filtered, concentrated by ultracentrifugation at 60,000 × g on an Optima XE-90 centrifuge with a SW 32 Ti rotor (Beckam Coulter), and stored at −80 °C. HEK 293T cells were exposed to lentivectors for 48 h, transfection efficiency was confirmed by E2 Crimson expression, then cells underwent flavivirus infection.

For imaging or molecular biology analyses, transient MITD1 and CHMP overexpression was achieved by transfection. pcDNA3.1-eGFP, pcDNA3.1-Myc-MITD1^{Hum}, pcDNA3.1-Myc-MITD1^{Bov}, pcDNA3.1-Myc-MIT, pcDNA3.1-Myc-ΔMIT, pcDNA3.1-CHMP1B-FLAG, pcDNA3.1-CHMP2A-FLAG, and pcDNA3.1-CHMP4B-FLAG were transfected in HEK 293T cells using PEI. Medium was changed 8 h posttransfection and GFP expression was assessed 48 h later.

Gene Knockdown. siRNAs targeting the transcripts encoding PPIB, SHFL, and MITD1 were ordered from Horizon Discovery as pools of four individual siRNAs (Dharmacon ON-TARGETplus SMARTpools) and transfected using HiPerFect Transfection Reagent (Qiagen), according to the manufacturer's instructions. Knockdown efficiency was evaluated by RT-qPCR 24 h posttransfection as previously described.

Mouse Experiments. Mouse experiments were previously described (64). Briefly, 6-d-old neonatal Swiss mice (Janvier Labs, France) were inoculated intraperitoneally with $10^4 \times TCID_{50}$/mouse of USUV. USUV-infected mice and control mice were killed with a lethal dose of pentobarbital (Merck) at 6 d postinfection. Liver, kidneys, spleen, and brain were snap frozen with liquid nitrogen and RNA was extracted using the RNeasy Mini kit (Qiagen) following the manufacturer's instructions. Mice were infected at E.C.E. (Etablissement Confiné d'Expérimentation), a level 3 animal facility of the University of Montpellier. Animals were killed if they showed deterioration of body condition score and drastic weight loss (i.e., over 20%).

Binding and Internalization Assay. Vero E6 cell monolayers were prechilled on ice for 5 min, then incubated with WNV or USUV (MOI of 20) for 1 h on ice to block the internalization of the viruses. We used 200 μg/mL Heparin (Merck) as a control. The cells were then washed three times with ice-cold PBS to remove unbound particles. Cell surface–bound viruses were analyzed by harvesting RNA at this step. Viral internalization was induced by adding warm medium and keeping the cells for 2 h at 37 °C. We used 50 μM PitStop2 (MedChemExpress) as a control. The cells were then treated with 0.25% Trypsin–EDTA for 15 min at 37 °C to remove uninternalized particles, cells were pelleted, washed three times with PBS, and RNA was harvested.

Confocal Microscopy. Cells were seeded on poly-D-lysine-coated glass coverslips. Cells were washed with PBS, then fixed with PBS, 4% PFA for 15 min. Cells were permeabilized with PBS, 0.5% Triton X-100 (Merck), and then blocked with PBS, 0.05% Tween 20 (Merck), and 1% BSA for 30 min. Cells were stained in PBS, 0.05% Tween 20 (Merck) and 1% BSA with primary antibodies for 2 h and secondary antibodies for 1 h (*SI Appendix*, Table S2). For membrane or lipid droplet studies, cells were stained with 1 μg/mL Nile Red in PBS for 15 min. Cells were furthermore stained with Hoechst 33342 (Thermo Fisher Scientific) following the manufacturer's instructions. Coverslips were washed with deionized water, and mounted onto a glass slide with ProLong Diamond antifade mountant (Thermo Fisher Scientific). Images were acquired on Airyscan LSM880 (Zeiss) confocal microscope equipped with a 63× objective, operated by Zen software. Images were analyzed with ImageJ.

Image Quantifications. Colocalization of MITD1 with dsRNA and Env was assessed by measuring one-dimensional fluorescence signals across a distance of ±15 μm, ensuring the path intersected more than three peaks of fluorescence, using the "plot profile" function in ImageJ. Three measurements were taken per image, and Pearson's *r* correlation coefficients were calculated.

Aggregation of ESCRT-III proteins was evaluated by measuring the stained area using the "analyze particles" function in ImageJ, considering only particles greater than 0.02 μm^2. Fields containing both transfected and untransfected cells were analyzed. A mask was generated using the Myc signal to distinguish between transfected and untransfected cells. The mean foci size was calculated for each image for both transfected and untransfected cells.

The number of viral replication factories per cell was quantified using the "find maxima" function in ImageJ, with a prominence threshold of 5,000 to count significant dsRNA spots, minimizing background noise. The number of cells per field was determined by manually counting Hoechst-stained nuclei. The average number of viral replication factories per cell was calculated for each condition.

Western Blot. Soluble protein extraction was performed with RIPA buffer (25 mM Tris-HCl [pH 7.5], 150 mM NaCl, 0.5% sodium deoxycholate, 1% NP-40, 1 mM EDTA, 2.5 mM sodium pyrophosphate, 1 mM sodium orthovanadate, and 1 mM β-Glycerophosphate) supplemented with protease inhibitor (complete mini EDTA-free protease inhibitor cocktail, Merck), for 15 min with periodic scraping, and centrifuged at 15,000 × g for 10 min to remove insoluble debris. Whole protein extraction was performed with sodium dodecyl sulfate (SDS) buffer (25 mM Tris-HCl [pH 7.5], 150 mM NaCl, 2% SDS) for 15 min with periodic scraping. Samples were heat-denatured at 95 °C for 10 min in 4× Laemmli buffer (250 mM Tris-HCl [pH 7], 8% SDS, 40% glycerol, 10% β-mercaptoethanol, and 0.005% bromophenol blue), underwent SDS polyacrylamide gel electrophoresis (SureCast Gel Handcast System, Thermo Fisher Scientific), followed by transfer onto a 0.45 μm nitrocellulose membrane (Amersham). Membranes were saturated in PBS, 0.05% Tween 20 (PBST) with 10% fat-free milk for 30 min. Primary antibodies and secondary antibodies (*SI Appendix*, Table S2) were diluted in PBST, 1% BSA. Primary antibodies were incubated for 16 h at 4 °C, and secondary antibodies for 2 h at room temperature, with three 5-min PBST washes between each step. Protein visualization was achieved by HRP activity (Immobilon Forte Western HRP substrate, Merck) on a ChemiDoc imaging system (Bio-Rad). Images were analyzed with ImageJ.

Immunoprecipitation. Soluble protein extraction was performed with RIPA buffer supplemented with protease inhibitor, for 15 min with periodic scraping, and centrifuged at 15,000 × g for 10 min to remove insoluble debris. Immunoprecipitation of Myc and FLAG tagged proteins were performed with nanobodies-coated agarose beads (Myc-Trap, DYKDDDDK Fab-Trap, GFP-Trap, and HA-Trap, ChromoTek) following the manufacturer's instructions.

Statistical Analyses. Graphical representations and statistical analyses were performed using GraphPad Prism software version 10 for Windows (GraphPad Software) except for the ISG arrayed expression screen, which was compiled and analyzed with R software version 4.4.1 for Windows. Statistical significance was assessed with *t* tests, one-way, and two-way ANOVA followed by the appropriate multiple comparison analysis (indicated in figure legends); normality tests were performed prior to analysis.

Ethics Statement. Mice were bred and maintained according to the French Ministry of Agriculture and European Institutional guidelines (Appendix A STE No. 123). Experiments were performed according to national regulations and approved by the regional ethics committee of Languedoc-Roussillon (Comité régional d'éthique sur l'expérimentation animale, Languedoc-Roussillon), France (Approval No. 6773 to 201609161356607).

Human fetuses were obtained after legal abortion with written informed consent from the patient. The procedure for the procurement and use of human fetal central nervous system tissue was approved and monitored by the "Comité Consultatif de Protection des Personnes dans la Recherche Biomédicale" of Henri Mondor Hospital, France. Declaration number at the French Research Ministry for the use of human neural progenitor cells is DC-2019-3771 (UMR Virology).

Data, Materials, and Software Availability. All study data are included in the article and/or supporting information.

ACKNOWLEDGMENTS. This work was supported by grants from the Agence Nationale de la Recherche (ANR-21-CE15-0041 to S.S. and S.N.) and the UK Medical Research Council (MC_UU_12014/10 to M.P. and S.J.W., MC_UU_00034/3 to M.P., MR/ K024752/1 to S.J.W., and MR/P022642/1 to S.J.W.). J.Z. was supported by a grant from the Agence Nationale de la Recherche (ANR-21-CE15-0041). M. Cannac and I.B. are recipients of doctoral grants from the French Ministry of Higher Education and Research. We acknowledge the imaging facility of Montpellier (MRI), member of the national infrastructure France-BioImaging supported by the Agence Nationale de la Recherche (ANR-10-INBS-04, "Investissements d'avenir"). This publication was supported by the European Virus Archive GLOBAL (EVA-GLOBAL) project that has received funding from the European Union's Horizon 2020 research and innovation program under grant agreement No 871029. We thank Andres Merits (University of Tartu, Estonia), Theodore Pierson (Vaccine Research Center, NIAID, Bethesda, MD), Olivier Moncorgé (Interferon and antiviral restriction team, IRIM, France), Cécile Boscheron and Winfried Weissenhorn (Institut de Biologie Structurale, Grenoble, France), and Odile Blanchet (CHU Angers, Centre de Ressources Biologiques, BB-0033-00038 Angers, France) for sharing reagents and cells.

Author affiliations: [a]Viral Trafficking, Restriction and Innate Signaling, CNRS UMR 9004, Institut de Recherche en Infectiologie de Montpellier, Université de Montpellier, Montpellier 34090, France; [b]Pathogenesis and Control of Chronic and Emerging Infections, INSERM, Établissement français du sang (EFS), Université de Montpellier, Montpellier 34394, France; [c]Medical Research Council-University of Glasgow Centre for Virus Research, Glasgow G61 1QH, United Kingdom; [d]Animal, Santé, Territoires, Risques et Ecosystèmes, UMR 117, Centre de coopération internationale en recherche agronomique pour le développement (CIRAD), Institut national de recherche pour l'agriculture, l'alimentation et l'environnement (INRAE), Université de Montpellier, Montpellier 34398, France; [e]UMR Virologie, Laboratoire de Santé Animale, Institut national de recherche pour l'agriculture, l'alimentation et l'environnement (INRAE), Anses, Ecole Nationale Vétérinaire d'Alfort, Maisons-Alfort 94700, France; and [f]Cambridge Institute of Therapeutic Immunology and Infectious Disease, Jeffrey Cheah Biomedical Centre, Department of Medicine, University of Cambridge, Cambridge CB2 0AW, United Kingdom

1. T. C. Pierson, M. S. Diamond, The continued threat of emerging flaviviruses. *Nat. Microbiol.* **5**, 796–812 (2020).
2. S. Mukhopadhyay, R. J. Kuhn, M. G. Rossmann, A structural perspective of the flavivirus life cycle. *Nat. Rev. Microbiol.* **3**, 13–22 (2005).
3. U. Ashraf *et al.*, Usutu virus: An emerging flavivirus in Europe. *Viruses* **7**, 219–238 (2015).
4. M. Clé *et al.*, Usutu virus: A new threat? *Epidemiol. Infect.* **147**, e232 (2019).
5. F. Roesch, A. Fajardo, G. Moratorio, M. Vignuzzi, Usutu virus: An arbovirus on the rise. *Viruses* **11**, 640 (2019).
6. D. Cadar, Y. Simonin, Human Usutu virus infections in Europe: A new risk on horizon? *Viruses* **15**, 77 (2022).
7. M. Graninger *et al.*, The first case of Usutu virus neuroinvasive disease in Austria, 2021. *Open Forum. Infect. Dis.* **9**, ofac255 (2022).
8. P. Gaibani *et al.*, Case report of Usutu virus infection in an immunocompromised patient in Italy, 2022. *J. Neurovirol.* **29**, 364–366 (2023).
9. C. M. Gill *et al.*, Usutu virus disease: A potential problem for North America? *J. Neurovirol.* **26**, 149–154 (2020).
10. S. E. Ronca, J. C. Ruff, K. O. Murray, A 20-year historical review of West Nile virus since its initial emergence in North America: Has West Nile virus become a neglected tropical disease? *PLoS Negl. Trop Dis.* **15**, e0009190 (2021).
11. D. Nash *et al.*, The outbreak of West Nile virus infection in the New York City area in 1999. *N. Engl. J. Med.* **344**, 1807–1814 (2001).
12. L. Sánchez-Lerma *et al.*, Unexpected arboviruses found in an epidemiological surveillance of acute tropical febrile syndrome in the department of Meta, Eastern Colombia. *J. Infect. Public Health* **17**, 102510 (2024).
13. C. Scagnolari *et al.*, Usutu virus growth in human cell lines: Induction of and sensitivity to type I and III interferons. *J. Gen. Virol.* **94**, 789–795 (2013).
14. G. Cacciotti *et al.*, Variation in interferon sensitivity and induction between Usutu and West Nile (lineages 1 and 2) viruses. *Virology* **485**, 189–198 (2015).
15. W. M. Schneider, M. D. Chevillotte, C. M. Rice, Interferon-stimulated genes: A complex web of host defenses. *Annu. Rev. Immunol.* **32**, 513–545 (2014).
16. J. W. Schoggins, Interferon-stimulated genes: What do they all do? *Annu. Rev. Virol.* **6**, 567–584 (2019).
17. D. Jiang *et al.*, Identification of five interferon-induced cellular proteins that inhibit west nile virus and dengue virus infections. *J. Virol.* **84**, 8332–8341 (2010).
18. Z. Zhou *et al.*, Antiviral activities of ISG20 in positive-strand RNA virus infections. *Virology* **409**, 175–188 (2011).
19. Y. Suzuki *et al.*, Characterization of RyDEN (C19orf66) as an interferon-stimulated cellular inhibitor against dengue virus replication. *PLoS Pathog.* **12**, e1005357 (2016).
20. R. B. Richardson *et al.*, A CRISPR screen identifies IFI6 as an ER-resident interferon effector that blocks flavivirus replication. *Nat. Microbiol.* **3**, 1214–1223 (2018).
21. A. Dukhovny *et al.*, A CRISPR activation screen identifies genes that protect against Zika virus infection. *J. Virol.* **93**, e00211-19 (2019).
22. I. N. Boys *et al.*, RTP4 is a potent IFN-inducible anti-flavivirus effector engaged in a host–virus arms race in bats and other mammals. *Cell Host Microbe* **28**, 712–723.e9 (2020).
23. F. Valdez *et al.*, Schlafen 11 restricts flavivirus replication. *J. Virol.* **93**, e00104-19 (2019).
24. J. W. Schoggins *et al.*, A diverse range of gene products are effectors of the type I interferon antiviral response. *Nature* **472**, 481–485 (2011).
25. K. Tabata *et al.*, Unique requirement for ESCRT factors in flavivirus particle formation on the endoplasmic reticulum. *Cell Rep.* **16**, 2339–2347 (2016).
26. C. Thepparit *et al.*, Dengue virus requires apoptosis linked gene-2-interacting protein X (ALIX) for viral propagation. *Virus Res.* **261**, 65–71 (2019).
27. P.-T.-H. Tran, A. I. Chiramel, M. Johansson, W. Melik, Roles of ESCRT proteins ALIX and CHMP4A and their interplay with interferon-stimulated gene 15 during tick-borne flavivirus infection. *J. Virol.* **96**, e0162421 (2022).
28. C. Liu *et al.*, Cellular ESCRT components are recruited to regulate the endocytic trafficking and RNA replication compartment assembly during classical swine fever virus infection. *PLoS Pathog.* **18**, e1010294 (2022).
29. A. Calistri, A. Reale, G. Palù, C. Parolin, Why cells and viruses cannot survive without an ESCRT. *Cells* **10**, 483 (2021).
30. N. Chotiwan *et al.*, Type I interferon shapes brain distribution and tropism of tick-borne flavivirus. *Nat. Commun.* **14**, 2007 (2023).
31. R. M. Pinto *et al.*, BTN3A3 evasion promotes the zoonotic potential of influenza A viruses. *Nature* **619**, 338–347 (2023).
32. A. Hardy *et al.*, The timing and magnitude of the type I interferon response are correlated with disease tolerance in arbovirus infection. *mBio* **14**, e00101-23 (2023).
33. M. Miyashita, H. Oshiumi, M. Matsumoto, T. Seya, DDX60, a DEXD/H box helicase, is a novel antiviral factor promoting RIG-I-like receptor-mediated signaling. *Mol. Cell Biol.* **31**, 3802–3819 (2011).
34. J. Zoladek, S. Nisole, Mosquito-borne flaviviruses and type I interferon: Catch me if you can! *Front. Microbiol.* **14**, 1257024 (2023).
35. J. Zoladek *et al.*, A specific domain within the 3′ untranslated region of Usutu virus confers resistance to the exonuclease ISG20. *Nat. Commun.* **15**, 8528 (2024).
36. S. Y. Kim *et al.*, Interaction of Zika virus envelope protein with glycosaminoglycans. *Biochemistry* **56**, 1151–1162 (2017).
37. M. Hoffmann, N. L. Snyder, L. Hartmann, Polymers inspired by heparin and heparan sulfate for viral targeting. *Macromolecules* **55**, 7957–7973 (2022).
38. M.-R. Ho *et al.*, Blockade of dengue virus infection and viral cytotoxicity in neuronal cells in vitro and in vivo by targeting endocytic pathways. *Sci. Rep.* **7**, 6910 (2017).
39. M. Li *et al.*, Characterization of Zika virus endocytic pathways in human glioblastoma cells. *Front. Microbiol.* **11**, 242 (2020).
40. T. C. Pierson *et al.*, A rapid and quantitative assay for measuring antibody-mediated neutralization of West Nile virus infection. *Virology* **346**, 53–65 (2006).
41. S. Lee *et al.*, MITD1 is recruited to midbodies by ESCRT-III and participates in cytokinesis. *Mol. Biol. Cell* **23**, 4347–4361 (2012).
42. M. A. Hadders *et al.*, ESCRT-III binding protein MITD1 is involved in cytokinesis and has an unanticipated PLD fold that binds membranes. *Proc. Natl. Acad. Sci. U.S.A.* **109**, 17424 (2012).
43. M. Vietri, M. Radulovic, H. Stenmark, The many functions of ESCRTs. *Nat. Rev. Mol. Cell Biol.* **21**, 25–42 (2020).
44. D. M. Wenzel *et al.*, Comprehensive analysis of the human ESCRT-III–MIT domain interactome reveals new cofactors for cytokinetic abscission. *Elife* **11**, e77779 (2022).
45. J. H. Hurley, P. I. Hanson, Membrane budding and scission by the ESCRT machinery: It's all in the neck. *Nat. Rev. Mol. Cell Biol.* **11**, 556–566 (2010).
46. P. Greenspan, E. P. Mayer, S. D. Fowler, Nile Red: A selective fluorescent stain for intracellular lipid droplets. *J. Cell Biol.* **100**, 965–973 (1985).
47. K. Zhanghao *et al.*, High-dimensional super-resolution imaging reveals heterogeneity and dynamics of subcellular lipid membranes. *Nat. Commun.* **11**, 5890 (2020).
48. S. Torii *et al.*, Host ESCRT factors are recruited during chikungunya virus infection and are required for the intracellular viral replication cycle. *J. Biol. Chem.* **295**, 7941–7957 (2020).
49. J. Bordignon *et al.*, Expression profile of interferon stimulated genes in central nervous system of mice infected with dengue virus Type-1. *Virology* **377**, 319–329 (2008).
50. S. Lesage *et al.*, Discovery of genes that modulate flavivirus replication in an interferon-dependent manner. *J. Mol. Biol.* **434**, 167277 (2022).
51. A. E. Shaw *et al.*, Fundamental properties of the mammalian innate immune system revealed by multispecies comparison of type I interferon responses. *PLoS Biol.* **15**, e2004086 (2017).
52. M. A. Samuel, M. S. Diamond, Alpha/beta interferon protects against lethal West Nile virus infection by restricting cellular tropism and enhancing neuronal survival. *J. Virol.* **79**, 13350–13361 (2005).
53. H. M. Lazear, A. K. Pinto, M. R. Vogt, M. Gale, M. S. Diamond, Beta interferon controls West Nile virus infection and pathogenesis in mice. *J. Virol.* **85**, 7186–7194 (2011).
54. E. Weber *et al.*, Type I interferon protects mice from fatal neurotropic infection with Langat virus by systemic and local antiviral responses. *J. Virol.* **88**, 12202–12212 (2014).
55. S. Seitz, P. Clarke, K. L. Tyler, Pharmacologic depletion of microglia increases viral load in the brain and enhances mortality in murine models of flavivirus-induced encephalitis. *J. Virol.* **92**, e00525-18 (2018).
56. S. Stonedahl, J. S. Leser, P. Clarke, K. L. Tyler, Depletion of microglia in an ex vivo brain slice culture model of West Nile virus infection leads to increased viral titers and cell death. *Microbiol. Spectr.* **10**, e00685-22 (2022).
57. A. H. H. van Boxel-Dezaire *et al.*, Major differences in the responses of primary human leukocyte subsets to IFN-beta. *J. Immunol.* **185**, 5888–5899 (2010).
58. S. Leviyang, Interferon stimulated binding of ISRE is cell type specific and is predicted by homeostatic chromatin state. *Cytokine: X* **3**, 100056 (2021).
59. A. Sekrecka *et al.*, Time-dependent recruitment of GAF, ISGF3 and IRF1 complexes shapes IFNα and IFNγ-activated transcriptional responses and explains mechanistic and functional overlap. *Cell Mol. Life Sci.* **80**, 187 (2023).
60. M. Lucas-Hourani *et al.*, Inhibition of pyrimidine biosynthesis pathway suppresses viral growth through innate immunity. *PLoS Pathog.* **9**, e1003678 (2013).
61. M. Fares *et al.*, Pathological modeling of TBEV infection reveals differential innate immune responses in human neurons and astrocytes that correlate with their susceptibility to infection. *J. Neuroinflammat.* **17**, 76 (2020).
62. C.-L. Chua, I.-C. Sam, A. Merits, Y.-F. Chan, Antigenic variation of East/Central/South African and Asian chikungunya virus genotypes in neutralization by immune sera. *PLOS Neglected Trop. Dis.* **10**, e0004960 (2016).
63. M. Kane *et al.*, Identification of interferon-stimulated genes with antiretroviral activity. *Cell Host Microbe* **20**, 392–405 (2016).
64. M. Clé *et al.*, Study of Usutu virus neuropathogenicity in mice and human cellular models. *PLoS Negl. Trop Dis.* **14**, e0008223 (2020).